Occupancy oscillation of honeycomb-lattice hard-core bosons under a pseudo-magnetic-field

Jiaojiao Guo and Huaiming Guo
School of Physics, Beihang University, Beijing 100191, China

We investigate the hardcore Bose-Hubbard model on a honeycomb lattice under a pseudo-magnetic field generated by triaxial strain using the quantum Monte Carlo (QMC) method. In the presence of strain, we construct a phase diagram that encompasses superfluid and solid phases at different fillings. Interestingly, we observe intriguing phenomena related to filling factors, including a solid phase with a filling of $\rho = 0.4912$. This solid phase is characterized by distinct sublattice occupancies separated by large domain walls. Additionally, within the superfluid region, we observe stripe phases where the occupancy of hardcore bosons exhibits oscillatory behavior. Finally, we employ linear spin-wave theory and derive the pseudo-Landau levels present in the excitation spectrum. Our findings not only provide valuable insights into the behavior of hardcore bosons in the presence of pseudo-magnetic fields, but they can also be experimentally realized using ultracold bosonic atoms confined in optical lattices.

I. INTRODUCTION

Recently, there has been significant progress in studying the use of mechanical deformation to modulate the electronic properties of quantum materials. This includes the exploration of magic-angle twisted bilayer graphene [1–4] and strained monolayer graphene [5,6]. The minute "magic-angle" twisting in bilayer graphene flattens the low-energy band, giving rise to the emergence of correlated insulating states and unconventional superconductivity [3,4]. Another intriguing effect of mechanical deformation is the generation of high-strength pseudo-magnetic fields. It is predicted that, by applying triaxial strain, uniform pseudo-magnetic fields exceeding 10 T could be achieved. This causes electrons to behave as if they were subjected to a real magnetic field, forming pseudo-Landau levels [5]. Subsequently, a strain-induced pseudo-magnetic field is experimentally observed in graphene nanobubbles formed on the surface of Pt. The pseudo-Landau levels corresponding these fields reached several hundred Tesla [6], greatly surpassing the magnetic field strengths currently achievable in the laboratory. So far, pseudo-magnetic field behaviors related to strains have been observed in various experimental setups. These include suspended graphene drumheads on SiO_2 insulating substrates [7], growing monolayer graphene on Rh foil [8] and SiC substrate [9], as well as placing graphene on nanostructures that were appropriately constructed [10].

To better generate pseudo-magnetic fields in planar sheets, various methods of engineering the corresponding strains have been proposed, including triaxial strain [5,11,12], bending graphene ribbons [13–15], uniaxial strain increasing linearly in the applied direction [16–18], uniaxial strain on a shaped graphene ribbon [19]. These proposals not only guide experimental studies but also reveal the unique aspects of pseudo-magnetic fields. For example, in the case of uniaxial strain, the pseudo-Landau levels do not remain flat like those induced by real magnetic fields; instead, they display linear

dispersion as a result of additional modification of the Fermi velocities by the strain [18].

The application of an external magnetic field generally does not influence electrically neutral particles. However, a pseudo-magnetic field generated by manipulating the hopping amplitudes can indeed have an impact on them. It has been shown that the interplay of weak, spatially varying in-plane strains and doped gradients can result in the Landau quantization of Bogoliubov quasiparticles in a broad spectrum of two-dimensional nodal superconductors [20,21]. Furthermore, the application of triaxial strain to the renowned Kitaev model leads to the emergence of Landau levels of Majorana fermions in spin-liquid phases [22]. For the antiferromagnetic Heisenberg model on a honeycomb lattice, triaxial strain produces evenly spaced pseudo-Landau levels, originating from the upper end of the magnon spectrum [23,24]. Similar effects can also be observed in antiferromagnetic honeycomb-lattice nanoribbons subjected to nonuniform uniaxial strain modulation [25].

The Bose-Hubbard model is a fundamental many-body Hamiltonian that can be used to describe interacting bosons in an optical lattice. Initially studied theoretically by Fisher *et al.*, it predicted a superfluid-insulator transition driven by the on-site repulsion [26]. In 2002, Greiner *et al.* experimentally observed this intriguing quantum phase transition in a cold-atom experimental setup [27]. Since then, numerous studies have been conducted on various lattices, including square [28], triangular [29], honeycomb [30–32], kagome [33], and dice [34] lattices. These lattices exhibit various interesting quantum phases, such as superfluid (SF), Mott insulator, and supersolid, along with rich phase transitions among them.

In this study, we investigate the effect of triaxial strain on the honeycomb lattice based on the hardcore Bose-Hubbard model. By applying strain, we construct a comprehensive phase diagram that encompasses various phases, including SF, commensurate solids, and Mott insulator. The characteristics of these phases strongly depends on the filling conditions. Of

particular interest is the emergence of an insulating phase at a filling factor of $\rho = 0.4912$, induced by the applied strain. This phase is distinguished by the presence of domain walls near the boundaries, which separate lattice points occupied in different sublattices. In the SF phase, the domain walls exhibit different periodicities at varying fillings and the occupation displays oscillatory behavior. Lastly, we utilize the linear spin-wave approximation to analyze the excitation spectrum above the solid state at the filling $\rho = 0.51$ and unveil equally spaced pseudo-Landau energy levels.

The organization of this paper is as follows. Section II introduces the exact model and calculation methods that we will utilize. Section III introduces the results of the QMC calculation. Section IV shows the results of the spin-wave approximation. The results are then further discussed and explained in Sec. V.

II. MODEL AND METHOD

We investigate the hardcore Bose-Hubbard model on a honeycomb lattice, where the unstrained Hamiltonian is given by

$$H = -t_0 \sum_{\langle i,j \rangle}(a_i^\dagger a_j + \text{H.c.}) + \sum_{\langle i,j \rangle} V n_i n_j - \mu \sum_i n_i, \quad (1)$$

where a_i ($a_i^\dagger$) represents the hardcore bosonic annihilation (creation) operator on site i; $n_i = a_i^\dagger a_i$ is the number operator of bosons; $\langle i, j \rangle$ runs over all nearest-neighbor (NN) pairs. The first term in Eq. (1) describes the NN hopping of bosons with an amplitude of t_0. The second term represents the strength of the NN interaction, denoted as V. The third term involves the chemical potential μ. Throughout this work, $t_0 = 1$ is set as the energy scale.

The hardcore Bose-Hubbard model in Eq. (1) is derived from the extended Bose-Hubbard model given by

$$\begin{aligned} H_{\text{BH}} = &-t_0 \sum_{\langle ij \rangle} b_i^\dagger b_j + \frac{U}{2} \sum_i n_i(n_i - 1) \\ &+ \sum_{\langle i,j \rangle} V n_i n_j - \mu \sum_i n_i, \end{aligned} \quad (2)$$

in the large-U limit [35,36]. In this limit, the bosonic operators $b_i^\dagger$, b_i are replaced by the hardcore ones $a_i^\dagger$, a_i, with an occupancy of 0 or 1 on each site, leading to the vanishing of the on-site interaction U. The hardcore bosons follow the commutation relation $[a_i, a_j^\dagger] = 0$ for sites $i \neq j$, and the anticommutation relation $\{a_i, a_i^\dagger\} = 1$ for a single site i.

Applying a triaxial strain in graphene can produce a uniform pseudo-magnetic field generated by modulating the hopping amplitudes, so it can be extended to boson systems which cannot feel the real magnetic field. We consider the physical properties of Bose-Hubbard model under a pseudo-magnetic field generated by triaxial strain on a honeycomb lattice. The strain changes the lattice position, which, in turn, changes the magnitude of the hopping parameter, which vary with the bond length according to the following formula:

$$t \to t_{\text{ij}} = t_0 e^{-\beta\left(\frac{d_{ij}}{a_0} - 1\right)}, \quad (3)$$

where a_0 is the lattice constant of the undeformed honeycomb lattice, β is the Grüneisen parameter. After adding strain, the bond length is $\boldsymbol{d}_{ij} = \boldsymbol{r}_i - \boldsymbol{r}_j$, where the position of an atom is given by $\boldsymbol{r}_i = \boldsymbol{r}_i^0 + \boldsymbol{u}$, where $\boldsymbol{r}_i^0$ is the equilibrium position and $\boldsymbol{u}(x, y) = [u_x(x, y), u_y(x, y)]$ is the displacement field.

The strain tensor is given by classical continuum mechanics as

$$\epsilon_{ij} = \frac{1}{2}[\partial_j u_i + \partial_i u_j], \quad i, j = x, y. \quad (4)$$

The length of the three nearest-neighbor bonds is $d_{ij} = a_0(1 + \Delta u_n)$, where

$$\Delta u_n = \sum_{i,j} \frac{a_n^i a_n^j}{a_0^2} \epsilon_{ij}, \quad (5)$$

where the nearest-neighbor vectors $\boldsymbol{a}_n$ are given by

$$\boldsymbol{a}_1 = a_0[0, 1], \quad \boldsymbol{a}_2 = \frac{a_0}{2}[-\sqrt{3}, -1], \quad \boldsymbol{a}_3 = \frac{a_0}{2}[\sqrt{3}, -1]. \quad (6)$$

The strain in the honeycomb lattice can generate the following gauge field:

$$\mathcal{A} = \frac{\beta}{2}\begin{pmatrix} \epsilon_{xx} - \epsilon_{yy} \\ -2\epsilon_{xy} \end{pmatrix}. \quad (7)$$

The displacement field of the triaxial strain on the honeycomb lattice is

$$\vec{u}(\mathbf{r}) = c(2xy, x^2 - y^2), \quad (8)$$

where c is the constant of strain strength. Here, we use a linear approximation for the exponential function in Eq. (3): $t_{\text{ij}} = t_0[1 - \beta(d_{ij}/a_0 - 1)]$. Therefore, the strain modifies the hopping amplitudes, causing them to vary spatially. Consequently, the strained Hamiltonian we will investigate becomes

$$H_s = -\sum_{\langle i,j \rangle} t_{ij}(a_i^\dagger a_j + \text{H.c.}) + \sum_{\langle i,j \rangle} V n_i n_j - \mu \sum_i n_i. \quad (9)$$

In comparison to the Hamiltonian in Eq. (1), only the hopping amplitudes in the first term are modified. Under triaxial strain, the perpendicular edge bonds have the minimum coupling value. Therefore, for a finite triangular system, there is a maximum strain strength, which is determined by the vertical boundary bond hopping strength of zero [37].

In the following discussions, we employ the approach of stochastic series expansion (SSE) QMC [38,39] with directed loop updates to study the model in Eq. (1). The SSE method expands the partition function in a power series and the trace is written as a sum of diagonal matrix elements. The directed loop updates make the simulation very effcient [40]. In the following calculation, we set the inverse temperature $\beta = 50$, which is low enough to obtain the ground-state properties of finite-sized systems. The computing system is a zigzag-boundary triangle flake of honeycomb lattice with a linear dimension of $L = 50$ (see Fig. 1).

III. QMC RESULTS

We employed the QMC method to calculate the phase diagram of the hardcore Bose-Hubbard model on a honeycomb lattice, both with and without strain. The total number of
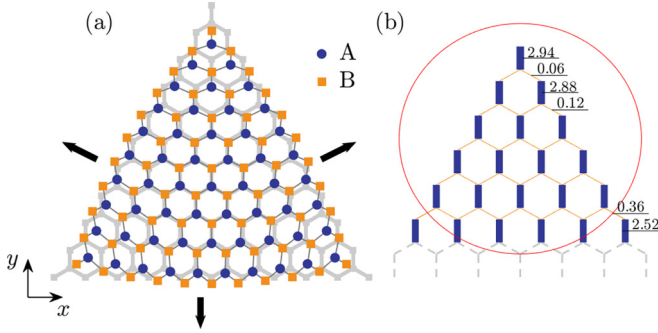
FIG. 1. (a) A deformed triangular-shaped honeycomb lattice with zigzag boundaries under triaxial strain. The lattice consists of L^2 sites, where the linear size is $L = 11$. The number of sites in sublattices A and B are not equal, with $N_A = L(L-1)/2$ and $N_B = L(L+1)/2$. (b) An enlarged view of the upper corner region of the triangular flake with a larger size of $L = 50$. The thickness of each connector line corresponds to the strength of the bond, while the value of the hopping amplitude is indicated near the corresponding bond. The strain strength used in (b) is $c/c_{\max} = 1$.

lattice sites in the triangular flake is $N = N_A + N_B = 2500$. This geometric structure leads to a difference in the number of lattice sites between the two sublattices, with $N_B - N_A = 50$. Initially, we calculate the phase diagram without strain. When the ratio t_0/V is small, a solid phase with density $\rho = 0.51$ emerged (enclosed by the gray dotted line in Fig. 2), where the sublattice with more lattice sites was occupied. As t_0/V increased, the system transitions into the superfluid phase.
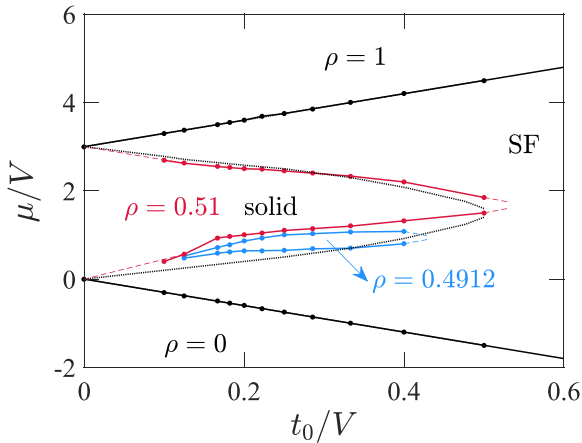

FIG. 2. Phase diagram of the ground state of the strained Bose-Hubbard model on a triangular flake with zigzag boundaries obtained by the QMC method, which includes two solid phases corresponding to densities of $\rho = 0.4912$ and $\rho = 0.51$, respectively. In the solid phase with density $\rho = 0.51$, only the sublattice with more lattice sites is occupied. The superfluid phases exist between the solid phases. Here, the solid lines in color represent the phase boundaries with strain, while the dashed lines in color are plotted to guide the eye in observing the trend of the corresponding solid lines. For comparison, the region of the $\rho = 0.51$ solid phase without strain is indicated by the gray dotted line. The upper (lower) black line separates the empty (full) state, which remains almost the same for both cases with and without strain.
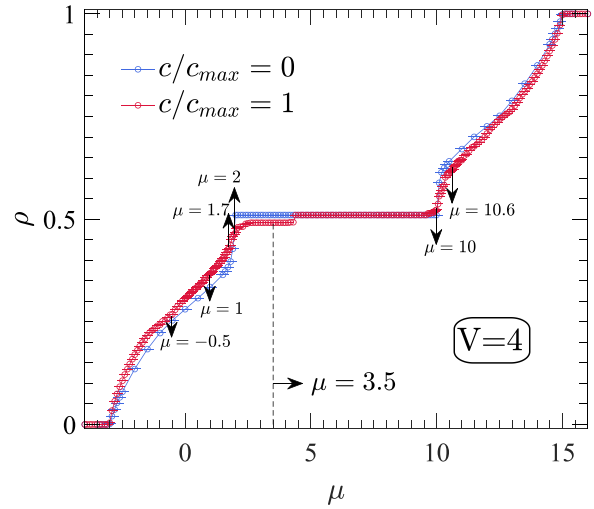

FIG. 3. The average density of the system as a function of μ at $V = 4$ for hardcore Bose-Hubbard on the honeycomb lattice. The blue line represents the case with strain, while the red line represents the case without strain. The vertical dashed line indicates the midpoint position of the platform with $\rho = 0.4912$. The positions marked by the arrows will be analyzed in detail in the subsequent figures.

Given that a single hardcore boson can hop to three NN sites on the honeycomb lattice, its energy is about $-3t_0$. The critical condition for a hardcore boson to enter the system is then given by $-3t_0 - \mu = 0$ (see the lower black line in Fig. 2). Consequently, no sites in the system were occupied for $\mu < -3t_0$, corresponding to an empty phase. Through a particle-hole transformation, the energy of introducing a single hole in the system is obtained as $-3(t_0 + V)$. Hence, each lattice site is filled with a boson for $\mu > 3(t_0 + V)$ (indicated by the upper black line in Fig. 2), resulting in a Mott insulating phase. Incorporating strain into the system had little effect on the phase boundaries of the $\rho = 0$ and $\rho = 1$ phases. However, it caused the plateau of the solid state with $\rho = 0.51$ to split into various plateaus with different filling densities. The density of these splitting plateaus can be universally expressed as $\rho = (N_A + 3p)/N$ (where p is the number of layers where the domain walls are located), and their values can be $\rho = 0.4912, 0.4924, 0.4936, \ldots$ ($p = 1, 2, 3, \ldots$). Each plateau has a vanishing compressibility $\kappa = \partial\rho/\partial\mu$, indicating a gapped system which we term as solid. Among these solids with the aforementioned fillings, except for the solid phase with $\rho = 0.4912$ which has a larger range, the ranges of the others are very small and thus not shown in the phase diagram. In addition to the solid phases, the remaining regions in the phase diagram are occupied by the superfluid phase.

The phase diagram in Fig. 2 is obtained from the average density accurately calculated by QMC

$$\rho = \frac{\sum_i n_i}{N_s}. \tag{10}$$

To gain a better understanding of the phase diagram depicted in Fig. 2, we examine how density changes with the chemical potential in the presence and absence of strain (see Fig. 3). In
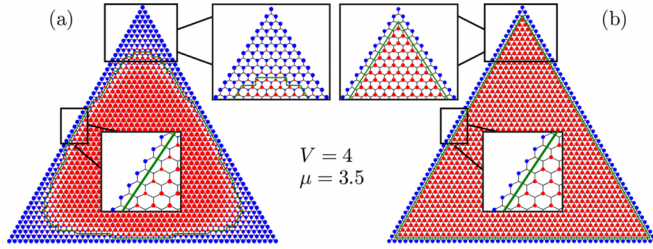
FIG. 4. (a) The local density distribution at $\mu = 3.5$, corresponding to a density of $\rho = 0.4912$. (b) An ideal filling configuration for $\rho = 0.4912$, featuring straight domain walls. The insets provide enlarged views of the highlighted regions in (a) and (b).
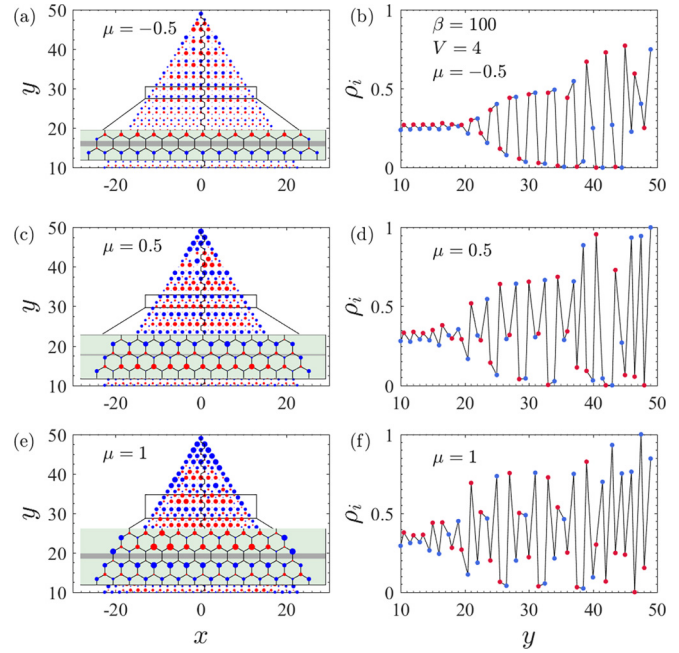

FIG. 5. The local density distribution in the upper corner of the triangular flake under different chemical potentials: (a) $\mu = -0.5$, (c) $\mu = 0.5$, and (e) $\mu = 1$. The insets provide enlarged views of the density distribution around the domain walls, which are depicted by gray lines. (b), (d), and (f) display the values of the local densities along the high-symmetry paths corresponding to (a), (c), and (e), respectively.

the absence of strain, there are only three plateaus: $\rho = 0$, $\rho = 0.51$, $\rho = 1$, which correspond to the incompressible insulating phases. The transition from the $\rho = 0.51$ solid phase to the superfluid is of first order. However, when strain is applied, the $\rho = 0.51$ density plateau splits into two separate plateaus with values $\rho = 0.4912$ and $\rho = 0.51$, respectively.

Next, we turn our attention to the plateau with a density of 0.4912 induced by strain and conduct a detailed analysis of the filling configuration in this solid phase, as shown in Fig. 4(a). It is clear that the central region of the geometry is occupied by bosons on the A sublattice, while the edge region is filled with bosons on the B sublattice. A distinct domain wall forms at the boundary between these two regions. To examine the precise shape of the domain wall, we zoom in on the configurations at two representative positions in the system: the center of the edge and the vicinity of the upper corner. Near the center of the boundary, the domain wall resides in the first layer, specifically on the outermost zigzag chain where bosons are filled on the B sublattice, while the remaining region is filled on the A sublattice. Near each corner, the domain wall lies inside, away from the corner, and exhibits a meandering shape.

To gain a deeper understanding of the solid phase corresponding to $\rho = 0.4912$, we can exclude quantum fluctuations stemming from the NN hoppings. In one ideal configuration (where each site is occupied by 0 or 1 hardcore boson) with all domain walls forming straight lines, a precise density of $\rho = 0.4912$ is achieved. As shown in Fig. 4(b), it can be seen that the outermost layer of bosons is filled on the B sublattice, and upon crossing the domain wall, the bosons are filled on the A sublattice in the remaining region. By gradually increasing the number of outer layers, densities of $\rho = 0.4924, 0.4936, \ldots$ can also be achieved successively. However, these relatively higher-density fillings have extremely small regions in the phase diagram and are numerically unstable. Further investigation into their properties has not been conducted. Therefore, we establish a direct relationship between the average density and the position of the domain wall. Additionally, it was observed that the meandering domain walls near the corners can be considered as deformations of ideal straight domain walls, which further reduce the energy of the system.

Interestingly, the introduction of strain also results in novel filling patterns in the superfluid phase, characterized by the presence of domain walls with varying sizes and numbers. These domain walls disrupt the uniformity of boson filling

and give rise to a pattern composed of smaller regions. The properties of the domain walls change as the filling factor varies. Figure 5 illustrates several local density profiles of the superfluid phase under different chemical potentials. Due to the three-fold rotational symmetry, only the configuration of the upper triangle part of the system is shown. In Fig. 5(a), the filling pattern at $\mu = -0.5$ is depicted, representing a situation where the average density is low and the system is in the superfluid state. In this case, most of the bosons are concentrated near the three corners and multiple domain walls are observed within the system. The width of these domain walls is narrow, spanning only two zigzag chains. Figure 5(b) displays the local density values along a high-symmetry path. The domain wall appears approximately within the range of $20 < y < 40$. Its presence is indicated by each pair of values approaching zero, and its location is between the two corresponding lattice sites. Figures 5(c) to 5(f) illustrate the results for $\mu = 0.5, 1$. As the chemical potential increases, the average density continues to rise, and the region occupied by bosons gradually expands towards the interior of the triangular flake. The number of domain walls begins to decrease, but their widths increase. For instance, at $\mu = 0.5, 1$, the domain wall regions encompass three and four zigzag chains, respectively.

Upon closer examination of higher fillings, we discover intriguing filling patterns near the phase boundary between the SF phase and the solid phases. Figure 6 displays the local density profile of the SF phase adjacent to the solid plateaus. The top row represents the filling before reaching the density
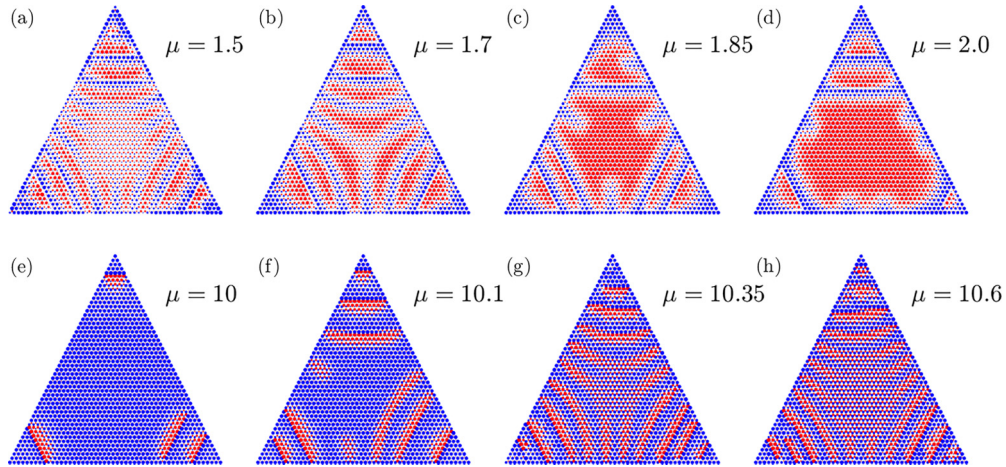
FIG. 6. The local density distribution in the superfluid phases with different chemical potentials: (a) $\mu = 1.5$, (b) $\mu = 1.7$, (c) $\mu = 1.85$, (d) $\mu = 2.0$, (e) $\mu = 10.0$, (f) $\mu = 10.1$, (g) $\mu = 10.35$, and (h) $\mu = 10.6$. Here the strain strength is $c/c_{\max} = 1$.

plateau of $\rho = 0.4912$, while the bottom row shows the filling after reaching the plateau of $\rho = 0.51$ (see the arrows in Fig. 3).

In Fig. 6, we observe curved stripes separated by domain walls forming in the system, with the number of stripes reaching its maximum at $\mu = 1.5$. At $\mu = 1.85$, the central region of the system exhibits a "fusion"-like filling behavior. This is characterized by a transition from blue-red streak filling in the lattice sites to solely red site filling, accompanied by a distinct turning point in the density curve, as depicted in Fig. 7. As the chemical potential increases to $\mu = 2$, the range of red point filling in the central region expands further, and the density value approaches $\rho = 0.4912$, indicating a tendency towards the split plateaus.

At $\mu = 10$, the average density of the system slightly surpasses the $\rho = 0.51$ plateau, resulting in a filling pattern characterized by several red stripes on the background of occupied blue lattice sites. With increasing chemical potential, the number of occupied red lattice sites and stripes continues to grow, as illustrated in Fig. 6(f) for $\mu = 10.1$. At $\mu = 10.35$, red stripes appear throughout the triangle flake. As the chemical potential further increases, the number of stripes expands and the red stripes in the central region start to merge. Ultimately, all red lattice sites are occupied, and the system becomes a $\rho = 1$ Mott insulator.

From the aforementioned filling process, it is evident that the system exhibits distinct behaviors at low and high densities. At low densities, straight domain walls emerge at the three corners, with smaller domain wall regions. Conversely, at higher filling densities, the system displays pronounced stripes, wherein the boundaries of these stripes act as domain walls. However, these domain walls are curved and exhibit varying thickness, with the thickest part situated at the center of the domain wall. To comprehend these discrepancies, we conducted further investigations into the density curve and discovered significant inflection points. Figure 7(a) depicts the results before solid phase at $\rho = 0.4912$, where the system is in the superfluid phase. Notably, the density curve exhibits a clear inflection point at $\mu = 1.85$. We computed the first-order derivative of the average density with respect to the chemical potential and observed its maximum value at $\mu = 1.85$, which aligns with the curve's inflection point. Similarly, Fig. 7(b) showcases the results after solid phase at $\rho = 0.51$. Near $\mu = 10.3$, the slope of the curve experiences a significant increase, and the maximum value of $\partial\rho/\partial\mu$ occurs at $\mu = 10.3$, consistent with the evolution of the filling patterns of the superfluid phase above $\rho = 0.51$.

Here, we only present the results at the strain strength $c_{\max}$, which generates a maximum pseudo-magnetic field and leads to the most pronounced phenomenon. The behavior at weaker strengths is similar, except the strain-induced modification is less apparent. For example, the split $\rho = 0.4912$ plateau in Fig. 3 is shortened, and the curved stripes in Fig. 6 become blurry.
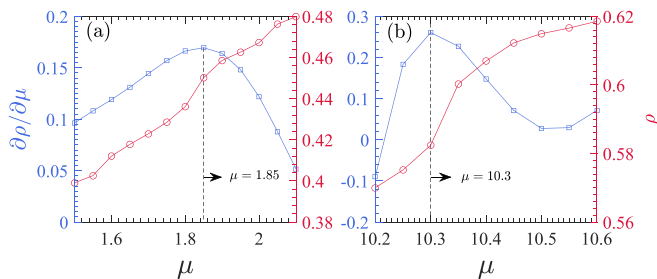

FIG. 7. The average density (red) and its derivative with respect to chemical potential (blue) in small ranges close to the solid phases with (a) $\rho = 0.4912$ and (b) $\rho = 0.51$.

IV. LINER SPIN-WAVE THEORY OF THE EXCITED STATE ABOVE THE SOLID $\rho = 0.51$

It is well known that linear spin-wave theory (LSWT) can be used to qualitatively analyze the properties of the model. In the following we will use LSWT to study the excited state behavior above the solid phase $\rho = 0.51$ under triaxial strain. By performing the following mapping $S_i^\dagger = b_i^\dagger$ and $S_i^Z = n_i - \frac{1}{2}$, the hardcore Bose-Hubbard model is equivalent to the XXZ model with spin $S = 1/2$. As is well known, spins obey the
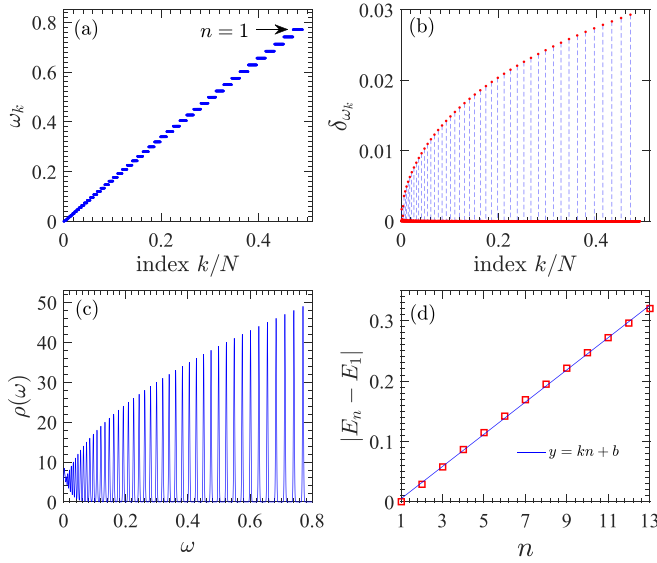
FIG. 8. (a) The magnon spectrum near the upper end of the energy spectrum as a function of the normalized index. (b) The corresponding difference between the adjacent eigenenergies. (c) The magnon density of states for the energy spectrum in (a). (d) The quantized PLLs measured relative to the first PLLs. The data are best fitted by a linear equation $y = kx + b$, with $k = 0.0267$, $b = -0.0213$. The linear size used here is $L = 50$.

following commutation relations

$$[S_{\alpha,i}, S_{\beta,j}] = i\hbar\varepsilon_{\alpha\beta\gamma}S_{\gamma,i}\delta_{ij}, \tag{11}$$

where $\varepsilon_{\alpha\beta\gamma}$ is the Levi-Civita symbol; α, β, $\gamma \in (x, y, z)$ represents the spin direction; and i and j denote the sites at which the spin is located. The filled sublattice corresponds to the spin-up state in the spin model. In the following, we consider lattice points filled only in the A sublattice. Under the Holstein-Primakoff transformation, the bosonic tight-binding Hamiltonian becomes

$$H = -\sum_{\langle i,j\rangle} t_{ij}(a_{i,A}a_{j,B} + a_{i,A}^\dagger a_{j,B}^\dagger)$$
$$+ (3V - \mu)\sum_{j\in B} a_{j,B}^\dagger a_{j,B} + \mu\sum_{i\in A} a_{i,A}^\dagger a_{i,A}. \tag{12}$$

Under the basis $X^\dagger = (a_1^\dagger, \ldots, a_{N_A}^\dagger, b_1, \ldots, b_{N_B})$, the Hamiltonian writes as $H = X^\dagger M X$, where M is a $N \times N$ matrix with $N = N_A + N_B$ being the total number of sites. Using the Bogolyubov transformation to diagonalize the matrix M, we obtain the magnon spectrum ω_k, then the density of state of the magnon can be further calculated

$$\rho(\omega) = \sum_k \delta(\omega - \omega_k) = \sum_k \frac{1}{\sqrt{2\pi}c_0}e^{-\frac{(\omega-\omega_k)^2}{2c_0^2}}, \tag{13}$$

where the δ function is approximated by a narrow Gaussian wave packet and c_0 is a small constant.

Figure 8(a) illustrates the magnon spectrum in a triangle flake of honeycomb lattice, which exhibits discrete degenerate energy levels. From the upper end of the spectrum, a series of almost flat energy levels can be observed. The

difference between adjacent energy eigenvalues is displayed in Fig. 8(b). The width of the energy plateau is represented by the distance between neighboring peaks, while the difference on the plateau tends to approach zero, indicating the near-flatness of the corresponding discrete energy levels. Figure 8(c) depicts the magnon density of states, where evenly spaced peaks are visible, indicating a nearly uniform gap between adjacent eigenenergy plateaus. Using the energy of the first PLL as the reference, we plot the relative energy of the nth-PLL as a function of n in Figs. 8(d). The resulting curve is observed to be best fitted by the equation $y = kx + b$ [$k = 0.0267$ and $b = -0.0213$], further confirming the equally spaced nature of the pseudo-Landau levels. These findings reveal that the application of strain induces the generation of a pseudo-magnetic field, resulting in the emergence of equally spaced magnon PLLs starting from the upper end of the energy spectrum.

V. CONCLUSION

We investigate the effects of triaxial strain on the hardcore Bose-Hubbard model in a triangular flake of a honeycomb lattice using QMC simulations. Upon the application of strain, the phase diagram exhibits superfluid and insulator phases at various filling factors. Notably, at an average density filling of $\rho = 0.4912$, a solid phase with distinct sublattice occupancies is observed, with a large domain wall separating the filled regions. Additionally, the superfluid phase in close proximity to the solid phase exhibits novel oscillating filling behaviors. By analyzing the excitation spectrum above the solid phase in the strained model, we discover an equally spaced pseudo-Landau levels within linear spin-wave theory.

The Bose-Hubbard model can be experimentally realized using cold atoms confined in an optical lattice. The creation of an artificial magnetic field is actively pursued in optical-lattice setups. Various schemes to generate gauge fields for ultracold atoms have been proposed and realized experimentally, such as the laser-assisted tunneling method and shaking the optical lattice [41–44]. Recently, in direct analogy with twisted and strained graphene, mechanical deformations have been extended to optical lattices. Twisted bilayer optical lattices have been experimentally realized, enabling the exploration of moiré physics of atomic Bose-Einstein condensates [45]. When it comes to strained optical lattices, several methods have been proposed to achieve them [46,47]. For instance, one proposal involves making slight modifications to existing experiments by displacing the beams with a standard configuration intersecting at $120°$ to generate the honeycomb lattice [46]. The spatial variations in beam intensities result in a corresponding spatial variation in lattice depth, thus enabling the acquisition of the hopping amplitudes needed for a uniform pseudo-magnetic field. Therefore, our findings, which showcase the behavior of hardcore bosons in the presence of pseudo-magnetic fields, can be experimentally realized by utilizing ultracold bosonic atoms confined in optical lattices.

ACKNOWLEDGMENTS

[1] R. Bistritzer and A. H. MacDonald, Proc. Natl. Acad. Sci. USA **108**, 12233 (2011).

[2] S.-Y. Li, K.-Q. Liu, L.-J. Yin, W.-X. Wang, W. Yan, X.-Q. Yang, J.-K. Yang, H. Liu, H. Jiang, and L. He, Phys. Rev. B **96**, 155416 (2017).

[3] Y. Cao, V. Fatemi, A. Demir, S. Fang, S. L. Tomarken, J. Y. Luo, J. D. Sanchez-Yamagishi, K. Watanabe, T. Taniguchi, E. Kaxiras, R. C. Ashoori, and P. Jarillo-Herrero, Nature (London) **556**, 80 (2018).

[4] Y. Cao, V. Fatemi, S. Fang, K. Watanabe, T. Taniguchi, E. Kaxiras, and P. Jarillo-Herrero, Nature **556**, 43 (2018).

[5] F. Guinea, M. Katsnelson, and A. Geim, Nat. Phys. **6**, 30 (2010).

[6] N. Levy, S. A. BurkeE, K. L. Meaker, and M. Panlasigui, Science **329**, 544 (2010).

[7] N. N. Klimov, S. Jung, S. Zhu, and T. Li, Science **336**, 1557 (2012).

[8] S.-Y. Li, K.-K. Bai, L.-J. Yin, J.-B. Qiao, W.-X. Wang, and L. He, Phys. Rev. B **92**, 245302 (2015).

[9] P. Nigge, A. C. Qu, E. Lantagne-Hurtubise, and E. Marsell, Sci. Adv. **5**, eaaw5593 (2019).

[10] C.-C. Hsu, M. L. Teague, J.-Q. Wang, and N.-C. Yeh, Sci. Adv. **6**, eaat9488 (2020).

[11] M. Neek-Amal, L. Covaci, K. Shakouri, and F. M. Peeters, Phys. Rev. B **88**, 115428 (2013).

[12] M. Settnes, S. R. Power, and A.-P. Jauho, Phys. Rev. B **93**, 035456 (2016).

[13] F. Guinea, A. K. Geim, M. I. Katsnelson, and K. S. Novoselov, Phys. Rev. B **81**, 035408 (2010).

[14] T. Low and F. Guinea, Nano Lett. **10**, 3551 (2010).

[15] D. B. Zhang and S. H. Wei, npj Comput. Math. **3**, 32 (2017).

[16] W.-Y. He and L. He, Phys. Rev. B **88**, 085411 (2013).

[17] Y.-H. Ho, E. V. Castro, and M. A. Cazalilla, Phys. Rev. B **96**, 155446 (2017).

[18] E. Lantagne-Hurtubise, X.-X. Zhang, and M. Franz, Phys. Rev. B **101**, 085423 (2020).

[19] S. Zhu, J. A. Stroscio, and T. Li, Phys. Rev. Lett. **115**, 245501 (2015).

[20] E. M. Nica and M. Franz, Phys. Rev. B **97**, 024520 (2018).

[21] G. Massarelli, G. Wachtel, J. Y. T. Wei, and A. Paramekanti, Phys. Rev. B **96**, 224516 (2017).

[22] S. Rachel, L. Fritz, and M. Vojta, Phys. Rev. Lett. **116**, 167201 (2016).

[23] M. M. Nayga, S. Rachel, and M. Vojta, Phys. Rev. Lett. **123**, 207204 (2019).

[24] J. Sun, N. Ma, T. Ying, H. Guo, and S. Feng, Phys. Rev. B **104**, 125117 (2021).

[25] J. Sun, H. Guo, and S. Feng, Phys. Rev. Res. **3**, 043223 (2021).

[26] M. P. A. Fisher, P. B. Weichman, G. Grinstein, and D. S. Fisher, Phys. Rev. B **40**, 546 (1989).

[27] M. Greiner, O. Mandel, T. Esslinger, T. W. Hansch, and I. Bloch, Nature (London) **415**, 39 (2002).

[28] P. Sengupta, L. P. Pryadko, F. Alet, M. Troyer, and G. Schmid, Phys. Rev. Lett. **94**, 207202 (2005).

[29] C. Becker, P. Soltan-Panahi, J. Kronjäger, S. Dörscher, K. Bongs, and K. Sengstock, New J. Phys. **12**, 065025 (2010).

[30] D.-S. Lühmann, O. Jürgensen, M. Weinberg, J. Simonet, P. Soltan-Panahi, and K. Sengstock, Phys. Rev. A **90**, 013614 (2014).

[31] S. Wessel, Phys. Rev. B **75**, 174301 (2007).

[32] J. Y. Gan, Y. C. Wen, J. Ye, T. Li, S.-J. Yang, and Y. Yu, Phys. Rev. B **75**, 214509 (2007).

[33] L. Santos, M. A. Baranov, J. I. Cirac, H.-U. Everts, H. Fehrmann, and M. Lewenstein, Phys. Rev. Lett. **93**, 030601 (2004).

[34] M. Rizzi, V. Cataudella, and R. Fazio, Phys. Rev. B **73**, 144511 (2006).

[35] I. Hen, M. Iskin, and M. Rigol, Phys. Rev. B **81**, 064503 (2010).

[36] M. Guglielmino, V. Penna, and B. Capogrosso-Sansone, Phys. Rev. A **84**, 031603(R) (2011).

[37] C. Poli, J. Arkinstall, and H. Schomerus, Phys. Rev. B **90**, 155418 (2014).

[38] O. F. Syljuåsen and A. W. Sandvik, Phys. Rev. E **66**, 046701 (2002).

[39] O. F. Syljuåsen, Phys. Rev. E **67**, 046701 (2003).

[40] F. Alet, S. Wessel, and M. Troyer, Phys. Rev. E **71**, 036706 (2005).

[41] Y.-J. Lin, R. L. Compton, K. Jiménez-García, J. V. Porto, and I. B. Spielman, Nature (London) **462**, 628 (2009).

[42] N. Goldman, G. Juzeliūnas, P. Öhberg, and I. B. Spielman, Rep. Prog. Phys. **77**, 126401 (2014).

[43] G. Jotzu, M. Messer, R. Desbuquois, M. Lebrat, T. Uehlinger, D. Greif, and T. Esslinger, Nature (London) **515**, 237 (2014).

[44] H. Miyake, G. A. Siviloglou, C. J. Kennedy, W. C. Burton, and W. Ketterle, Phys. Rev. Lett. **111**, 185302 (2013).

[45] Z. Meng, L. Wang, W. Han, F. Liu, K. Wen, C. Gao, P. Wang, C. Chin, and J. Zhang, Nature (London) **615**, 231 (2023).

[46] B. Tian, M. Endres, and D. Pekker, Phys. Rev. Lett. **115**, 236803 (2015).

[47] M. Jamotte, N. Goldman, and M. Di Liberto, Commun. Phys. **5**, 30 (2022).